frontiers | Frontiers in Earth Science

TYPE Original Research
PUBLISHED 05 July 2023
DOI 10.3389/feart.2023.1200779

OPEN ACCESS

EDITED BY
Xin Wang,
Hunan University of Science and Technology, China

REVIEWED BY
Irfan Rashid,
University of Kashmir, India
Andrew Jonathan Hodson,
The University Centre in Svalbard, Norway

*CORRESPONDENCE
Grace L. Brown,
g.l.brown@northumbria.ac.uk

RECEIVED 05 April 2023
ACCEPTED 23 June 2023
PUBLISHED 05 July 2023

CITATION
Brown GL and Brock BW (2023), Carbon flux in supraglacial debris over two ablation seasons at Miage Glacier, Mont Blanc massif, European Alps.
Front. Earth Sci. 11:1200779.
doi: 10.3389/feart.2023.1200779

Carbon flux in supraglacial debris over two ablation seasons at Miage Glacier, Mont Blanc massif, European Alps

Grace L. Brown* and Ben W. Brock

Department of Geography and Environmental Sciences, Northumbria University, Newcastle upon Tyne, United Kingdom

The cryosphere plays an important role in the global carbon cycle, but few studies have examined carbon fluxes specifically on debris-covered glaciers. To improve understanding of the magnitude and variability of the atmospheric carbon flux in supraglacial debris, and its environmental controls, near-surface CO_2 fluxes and meteorological variables were monitored over thick (0.23 m) and thin (0.04 m) debris at Miage Glacier, European Alps, over two ablation seasons, using an eddy covariance system. The CO_2 flux alternates between downward and upward orientation in the day and night, respectively, and is dominated by uptake of CO_2 in thick debris (mean flux = 1.58 g CO_2 m^{-2} d^{-1}), whereas flux magnitude is smaller and near net zero on thin debris (mean flux = −0.06 g CO_2 m^{-2} d^{-1}). These values infer a potential drawdown of >150 t CO_2 km^{-2} over an ablation season, and >500 t CO_2 (0.5 Gg CO_2) for the whole debris-covered zone. The strong correlation of daytime CO_2 flux magnitude with debris surface temperature suggests that atmospheric CO_2 is consumed in hydrolysis and carbonation reactions at sediment-water interfaces in debris. Incoming shortwave radiation is key in heating debris, generating dilute meltwater, and providing energy for chemical reactions. CO_2 drawdown on thin debris increases by an order of magnitude on days following frost events, implying that frost shattering generates fresh reactive sediment, which is rapidly chemically weathered with the onset of ice melting. Net CO_2 release in the night, and in the daytime when debris surface temperature is below 7°C, is likely due to respiration by debris microorganisms. The combination of dilute meltwater, high temperature, and reactive mineral surfaces open to the atmosphere, makes supraglacial debris an ideal environment for rock chemical weathering. Debris-covered glaciers could be important to local and regional carbon cycling, and measurement of CO_2 fluxes and controlling processes at other sites is warranted.

KEYWORDS

debris-covered glacier, carbon cycle, CO_2 flux, chemical weathering, microbial respiration, Miage Glacier, eddy covariance

1 Introduction

The global extent of supraglacial rock debris has been estimated as 29,183 km^2, equivalent to about 7% of total mountain glacier area, with prominent cover in High Mountain Asia, the Andes, Alaska, and the Arctic (Herreid and Pellicciotti, 2020). Debris-covered glaciers (DCGs), defined as having continuous debris cover across a large part of their ablation zone (Kirkbride, 2011) are present in most of the world's glacierised mountain

ranges, and their global area is expected to increase as climate warms (Scherler et al., 2018; Tielidze et al., 2020). Recent studies have demonstrated the distinctive influence of supraglacial debris on glacier mass balance and climatic response (Scherler et al., 2011; Fyffe et al., 2014; Rowan et al., 2015; Nicholson et al., 2021; Rounce et al., 2021; Wang et al., 2023), glacier hydrology (Gulley and Benn, 2007; Benn et al., 2017; Fyffe et al., 2019a; 2019b; Miles et al., 2020) and hazards (Benn et al., 2012; Watson et al., 2016; Racoviteanu et al., 2022). Hitherto, studies of carbon fluxes on glaciers have focused on biogeochemical processes either in cryoconite on the surface of "clean" glaciers (defined here as glaciers with no, or small amounts of discontinuous, surface debris) (Hodson et al., 2007; Anesio et al., 2009) or aquatic environments at the beds of glaciers and ice sheets (Hodson et al., 2000; Wadham et al., 2010; Graly et al., 2017; Wadham et al., 2019). At the surface of DCGs, the exposure of fresh mineral surfaces by mechanical weathering (Benn and Evans, 2010), availability of meltwater (Brock et al., 2010), and presence of diverse microbial populations (Gobbi et al., 2011; Franzetti et al., 2013; Darcy et al., 2017), makes the operation of biogeochemical processes involving CO_2 exchange with the atmosphere very likely. To date, however, direct measurements of carbon gas fluxes over supraglacial debris have been limited (Wang et al., 2014; Wang and Xu, 2018).

In subglacial environments, atmospheric CO_2 is an important source of aqueous protons, which facilitate key hydrochemical reactions at the beds of glaciers and ice sheets (Raiswell, 1984; Graly et al., 2017; Shukla et al., 2018; Wadham et al., 2019). Comminuted sediment (rock flour) created by crushing and grinding of rock at the glacier bed is highly geochemically reactive in suspension (St Pierre et al., 2019; Wadham et al., 2019). Carbonate and silicate hydrolysis dominate the initial rock-water reactions (Tranter et al., 1993) leading to an increase in pH and reduction of $p(CO_2)$ in the meltwater (e.g., Fairchild et al., 1994). This results in a steepening of the atmosphere-meltwater CO_2 gradient, driving diffusion of CO_2 into solution, and removing CO_2 from the lower atmosphere (Brown, 2002). Subsequent carbonation reactions can maintain low $p(CO_2)$ waters if reaction rates are sufficiently high (Tranter et al., 1993, Tranter et al., 2002) sustaining drawdown of atmospheric CO_2. In closed subglacial environments, isolated from the atmosphere, microbially-mediated oxidation of sulphide minerals and organic matter may replace CO_2 diffusion as a proton source (Sharp et al., 1999; Wadham et al., 2010) which could increase $p(CO_2)$ through microbial respiration. Supraglacial debris is an atmosphere-sediment-meltwater nexus which could be considered analogous to "open system" subglacial environments, in which mass movement and freeze thaw action would replace crushing and grinding in the production of comminuted sediment. Fyffe et al. (2019a) found elevated bicarbonate levels in supraglacial streams draining the lower debris-covered part of Miage Glacier, European Alps, compared with streams further upglacier, which drained mainly clean ice areas. The authors hypothesised that meltwater flowing through the debris matrix had become enriched with bicarbonate through hydrolysis reactions. It is therefore probable that supraglacial debris is an important, but little studied, geochemical sink of atmospheric CO_2 (Wang and Xu, 2018).

At the surface of clean glaciers and ice sheets, cycling of CO_2 between the surface and atmosphere is driven by microbial activity (Wadham et al., 2019). Studies in Greenland have identified consumption of atmospheric CO_2 by autotrophs in cryoconite (Hodson et al., 2008; Anesio et al., 2009; Anesio et al., 2010) and photoautotrophic algae in surface weathering crusts (Yallop et al., 2012) as dominant processes, with the potential to fix in the order of 10^4 kg C per km^{-2} as cryoconite in marginal areas of the Greenland Ice Sheet (Cook et al., 2012). Rates of photosynthesis and respiration are likely to be more closely balanced on Arctic valley glaciers, however (Telling et al., 2012). DCGs host a greater diversity of microbial life compared with clean ice and snow due to the presence of allochthonous material, sourced from nearby mountain slopes, which can accelerate microbial activity and the development of new soil in the debris layer (Franzetti et al., 2013; Azzoni et al., 2015). Soil dwelling communities of bacteria, fungi, Archaea, microfauna, and arthropods have been identified on DCGs (Franzetti et al., 2013; Azzoni et al., 2015). Studies on DCGs in the Italian Alps and Alaska Range found that microbial communities transitioned from heterotrophic to photosynthetic, and decreased in complexity, with increasing distance from the glacier terminus (Franzetti et al., 2013; Darcy et al., 2017) although their distribution also correlated with nutrient and water availability (Darcy and Schmidt, 2016). This implies that respiration, and release of CO_2 to the atmosphere, by microbes, microfauna and arthropods, will dominate over carbon drawdown by autotrophs in old and stable debris covers on the lower parts of DCGs, particularly where ablation is suppressed by thick debris cover (Franzetti et al., 2013). Photosynthesis by trees, shrubs and grasses growing on stable low-elevation areas of debris (Caccianiga et al., 2011) may also be locally influential to surface carbon exchange.

Eddy covariance (EC) is a micrometeorological method enabling direct measurement of surface turbulent fluxes through calculation of the covariance of the vertical wind velocity with fluctuations of the physical quantity under consideration. Instrumentation typically consists of a 3D sonic anemometer and infrared gas analyser measuring densities of H_2O and CO_2, together with a datalogger-software system capable of recording and processing high frequency measurements at 10 Hz or greater. EC systems have been widely deployed over vegetated surfaces in the past 2 decades and are seen as key to estimating long-term net ecosystem exchange of CO_2, (Baldocchi, 2019). The remoteness and harsh environment on glaciers have historically limited their application there, however, improvements in power supply technology and the portability and robustness of EC instrumentation have seen increasing application on glaciers (Nicholson and Stiperski, 2020). A small number of studies have deployed EC systems on DCGs, principally to provide direct measurements of the turbulent fluxes of sensible and latent heat, or to investigate boundary layer turbulence structures (Collier et al., 2014; Yao et al., 2014; Steiner et al., 2018; Nicholson and Stiperski, 2020). In a pioneering study, Wang and Xu (2018) deployed an EC system to measure vertical CO_2 fluxes directly over a debris-covered area of Koxkar Glacier, China, over a 2-year period. They calculated an average downward CO_2 flux of 58.68 mmol m^{-2} day^{-1} (equivalent to 2.58 g m^{-2} day^{-1}). This high rate of drawdown was attributed to consumption of CO_2 in

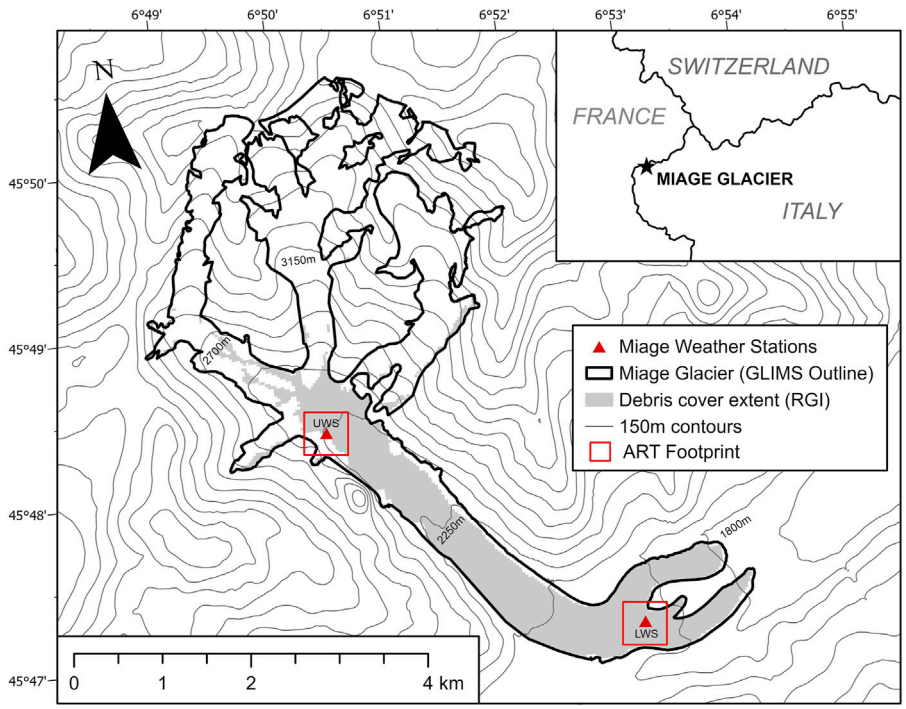

FIGURE 1
Site map of Miage Glacier showing weather station locations (LWS = lower weather station and UWS = upper weather station). The symbology of the weather stations reflects the grids shown in Figure 2. The insert shows the regional location of the study area. Contours produced using Copernicus data and information funded by the European Union—EU-DEM layers. https://www.eea.europa.eu/data-and-maps/data/copernicus-land-monitoring-service-eu-dem.

hydrochemical weathering reactions in debris. Sloping surfaces, inhomogeneous terrain, and presence of a low-level wind jet in katabatic flows present challenges to EC measurements on glaciers (Nicholson and Stiperski, 2020). The reliability of EC measurements of water vapour and CO_2 fluxes in complex alpine terrain has been investigated by Hiller et al. (2008) who concluded that EC systems are suitable for CO_2 flux measurements when placed within a suitable location within the study environment considering wind direction and local topography.

To date, the significance of DCGs, as a widespread and distinct glacier surface type, to terrestrial CO_2 fluxes has not been considered directly. Measurements are limited (Wang et al., 2014; Wang and Xu, 2018) and consequently little is known about the spatial and temporal variations of CO_2 flux magnitude on DCGs and its environmental controls. To address these questions, in this study we analyse a new dataset of EC measurements of CO_2 fluxes at two contrasting sites on an alpine DCG, over two summer ablation seasons. The EC data are analysed together with simultaneous measurements of meteorological variables and surface conditions from the same sites. The main aims are: i) to characterise the variability of CO_2 fluxes at hourly, daily, and seasonal scales, at sites representative of both thick and thin debris covers; and ii) to identify the likely controls on CO_2 flux variation in terms of independent environmental variables. It is concluded that thick debris cover is an important sink of atmospheric CO_2, with drawdown rates substantially higher than other glacial environments.

2 Materials and methods

2.1 Study site

Miage Glacier (Figure 1), located on the southern side of the Mont Blanc massif in the western Italian Alps (45°47′N, 06°52′E), has a total area of 10.5 km^2 and an elevation range of 1,740–4,640 m above sea level (a.s.l.) (Fyffe et al., 2014). The lowest 5 km^2 of the glacier, below approximately 2,500 m a.s.l., is almost completely covered by coarse, angular rock debris, dominated by mica-schists, gneiss, and granite, with smaller amounts of amphibolite, slate, fault breccia, quartzites and limestone, with iron oxidation common (Deline, 2002; Franzetti et al., 2013). Debris thickness increases downglacier from a thin and patchy cover <0.10 m thick in the upper ablation zone, to >0.50 m on the terminal lobes, and thickness is predominantly in the range 0.20–0.40 m over large areas of the tongue (Mihalcea et al., 2008; Foster et al., 2012) except for isolated blocks and debris mounds which may exceed 10 m thickness (Deline, 2009). The debris primarily originates from rockfalls and mixed snow and rock avalanches from the surrounding valley walls (Deline, 2009) and melt out of englacial debris forming moraines in the ablation area (Deline et al., 2012). In vertical profile, debris cover typically exhibits downward fining from an open-work cobble/boulder layer at the surface, through pebbles and granules, to sands and silts at the debris-ice interface. Brock et al. (2010) recorded mean ablation season melt rates ranging from 33 mm water equivalent (w.e.) d^{-1} beneath 0.04 m of debris to 6 mm w.e. d^{-1}

TABLE 1 Eddy covariance sensor specifications and accuracy.

Sensor	Manufacturer	Outputs	Accuracy/Error	Range	Precision
CSAT3	Campbell Scientific	u_x, u_y, u_z[a] (m s^{-1})	Offset errors	u_x ± 30 m s^{-1}	u_x 1 mm s^{-1} rms
			< ±8.0 cm/s (u_x, u_y)	u_y ± 60 m s^{-1}	u_y 1 mm s^{-1} rms
			< ±4.0 cm/s (u_z)	u_z ± 8 m s^{-1}	u_z 0.5 mm s^{-1} rms
			Gain error		
			±2% of reading (wind vector within ±5° of horizontal)		
EC150	Campbell Scientific	CO_2 Density (mg m^{-3})	Zero max drift: ±0.55 mg m^{-3} (±0.3 µmol mol°C^{-1})	0 to 1,000 µmol/mol	0.2 mg m^{-3} (0.5 µm mol^{-1})
		CO_2 Signal strength (0–1.0)	Gain drift: ±0.1%°C^{-1}		

[a](u_x, u_y, u_z are wind components referenced to the anemometer axes).

beneath 0.55 m debris, with the lowest layers of debris normally saturated with water during the ablation season. Temperatures over the debris-covered area were almost continuously positive in the June-September period, with frosts at the debris surface recorded on average only every 10 nights, although decreasing temperature with depth implies that frosts could be more frequent at the base of the debris layer at the ice interface. Fyffe et al. (2019b) recorded surface streams draining debris-covered sub-catchments, supplied by meltwater flowing through the base of the debris matrix. This observation implies a dynamic water table in debris, rising in the morning as dilute meltwater floods the lower layers, and falling during the evening and overnight due to declining melt rates and drainage. Furthermore, Brock et al. (2010) recorded daytime evaporation rates over debris as high as 1 mm h^{-1} suggesting that capillary action draws liquid water upwards into the warmer open-work cobble layers, which are open to atmospheric turbulence. Debris cover is highly mobile on moraine slopes and in the vicinity of streams and ice cliffs, and its distribution is intimately linked to spatial patterns of surface ablation (Fyffe et al., 2014; 2020; Westoby et al., 2020).

2.2 CO_2 gas flux measurement

Direct measurement of the near-surface vertical CO_2 flux in mg m^{-2} s^{-1}, F_c, was made using an open-path eddy covariance system, referred to as the EC system hereafter, consisting of a CSAT3 three-dimensional sonic anemometer and an EC150 CO_2/H_2O open path infra-red gas analyser, supplied by Campbell Scientific Ltd., Loughborough, United Kingdom (Table 1). The principles of trace gas flux measurement over glaciers using EC systems have been explained elsewhere, e.g., Wang and Xu (2018), and so are not repeated here. The EC system was installed at two separate sites in two different years to examine F_c variation over differing debris thickness and elevation: i) a lower weather station (LWS) at 2,000 m a.s.l., with mean debris thickness of 0.23 m, typical of the relatively thick debris present over much of the lower glacier, in the 2013 ablation season; and ii) an upper weather station (UWS) at 2,380 m a.s.l, with mean debris thickness of 0.04 m, representative of thin debris on the upper part of the continuously debris covered zone, in the 2016 ablation season. Both sites were located at the centre of level areas of the glacier surface, with little elevation variation within ~50 m of the LWS, and ~10 m of the UWS, with an upglacier slope of ~6° starting at a distance >10 m from the UWS (Figure 2). Surface debris around the measurement sites was mainly in the size range 0.10–0.40 m (long axis), with occasional boulders >1 m, at the LWS, and mainly <0.05 m (long axis) at the UWS. EC instruments were mounted surface parallel on cross arms at 1.83 m height, attached to a free-standing tripod, and oriented towards the dominant wind direction (westerly at the LWS and north-westerly at the UWS) to minimise airflow shadowing by the tripod and the mounting apparatus. The measurement height at a little below 2 m was considered a suitable distance from the surface to capture dominant turbulent eddies in the airflow, whilst not seriously violating the assumption of the constant flux layer. Previous work at the LWS site revealed an absence of katabatic flows, due to convection from the debris cover, with the wind speed maximum normally located above 2 m from the surface (Brock et al., 2010).

EC measurements were conducted between 26th June and 6th September 2013 at the LWS, and 24th June and 8th September 2016 at the UWS. 20 Hz measurements were recorded on a Campbell Scientific CR3000 datalogger and processed into 30-min averages using Campbell Scientific Open Path Eddy Covariance software (www.campbellsci.com). Corrections to the raw data were applied as follows: removal of unreliable values using sonic anemometer and gas analyser diagnostic codes; removal of low signal strength values (<90% full signal); lagging of CO_2 measurements against sonic wind measurements using a covariance maximisation procedure; and application of the "WPL" flux correction for air density fluctuations (Webb et al., 1980). Outlying values in the 30-min averages, defined as F_c fluxes greater than +/- 3 standard deviations about the mean, were also removed prior to further analysis. The majority of removed data were due to: i) rain or condensation lying on the sensor nodes reducing signal strength; and ii) data gaps due to power or logger failures, in particular between 16 July and 10 August 2013. The number of remaining half hour values were 1,941 at the LWS and 2,928 at the UWS. Measurement sites were monitored every 1–2 days in late June, early July, and early September, and on 1 day in early August, and minor adjustments made to level instruments due to differential ablation beneath the tripod feet.

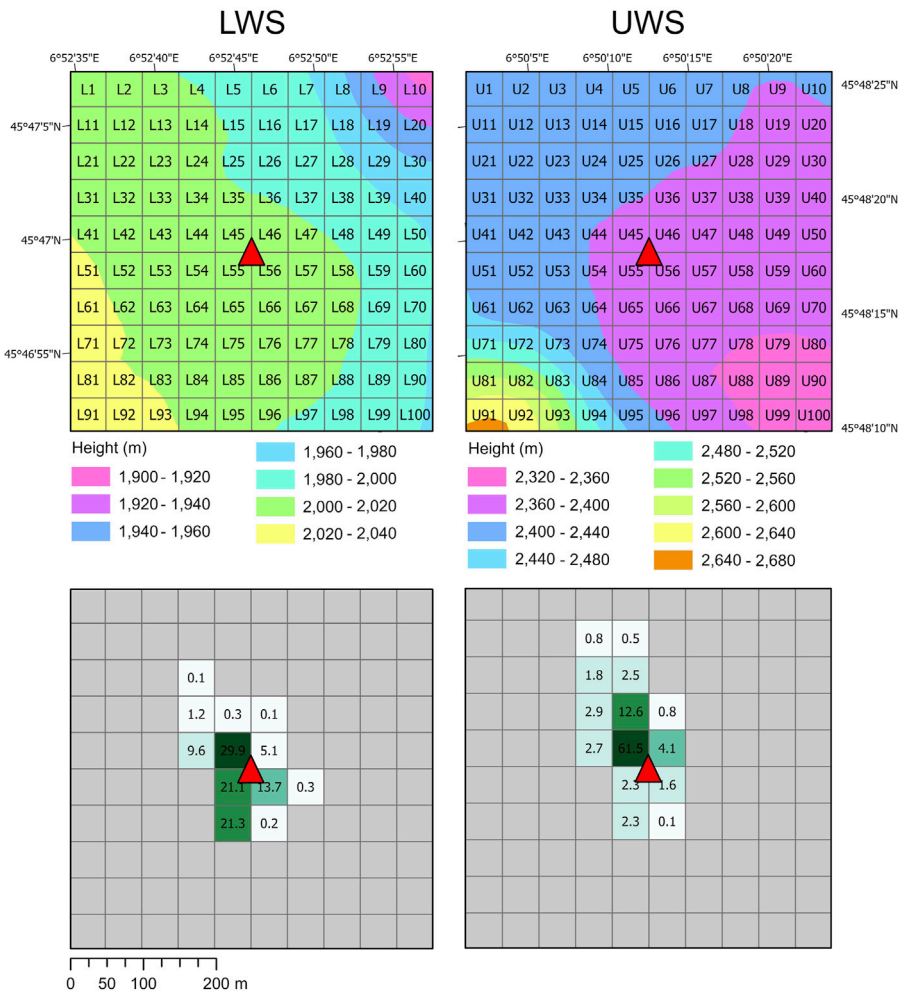

FIGURE 2
Spatial distribution of surface elevation (top row) and CO_2 footprint contribution from ART model runs (bottom row) in 50 × 50 m cells around the LWS (left column) and UWS (right column). The location of the weather stations is denoted by the red triangle.

Under stable atmospheric conditions with low wind speed, turbulent mixing may be insufficient for CO_2 absorbed or released at the surface to reach the instrument level. Estimation of the sub-instrument CO_2 storage is an important consideration in ecological studies where instrument heights are typically several metres above the vegetation surface and biological activity and surface roughness are high. However, over supraglacial debris, unstable atmospheric conditions dominate during ablation periods and wind speeds are high and sustained, even during the night (Brock et al., 2010). Only 0.3% of the total half hour records had a friction velocity <0.05 m s^{-1}, and no records had a friction velocity <0.01 m s^{-1}, indicating that periods of weak turbulent mixing were rare. Wang and Xu (2018) identified the daily atmospheric CO_2 storage in the debris area of Koxkar glacier to be less than 1% of net glacier carbon exchange, which they attributed to the low instrument height (2 m) limiting space for CO_2 storage and the porous nature of the surface material. Due to the low likelihood of substantial surface CO_2 storage, it was not considered in analysis of F_c in this study.

2.3 Measurement of independent meteorological variables

Both EC measurement sites were equipped with additional meteorological sensors to enable analysis of F_c variations using independent environmental variables. Air temperature, T_a (°C), and relative humidity (%) were measured using a HMP45C temperature and relative humidity sensor, housed inside a naturally ventilated Met21 radiation shield (both Campbell Scientific Ltd.). The Met21 radiation shield has been shown to be effective at protecting temperature sensors from anomalous solar heating on a debris-covered glacier (Shaw et al., 2016). The 4 components of the surface radiation balance (incident and reflected shortwave radiation, $S\downarrow$ and $S\uparrow$, respectively, and incoming and outgoing longwave radiation, $L\downarrow$ and $L\uparrow$, respectively; all in units of W m^{-2}) were measured using Kipp and Zonen CNR1 (LWS) and CNR4 (UWS) radiometers. All instruments were mounted at 1.83 m, except the radiometers, which were mounted at 1.6 m. The instrument setup was very similar to that described in Brock et al. (2010) and full sensor

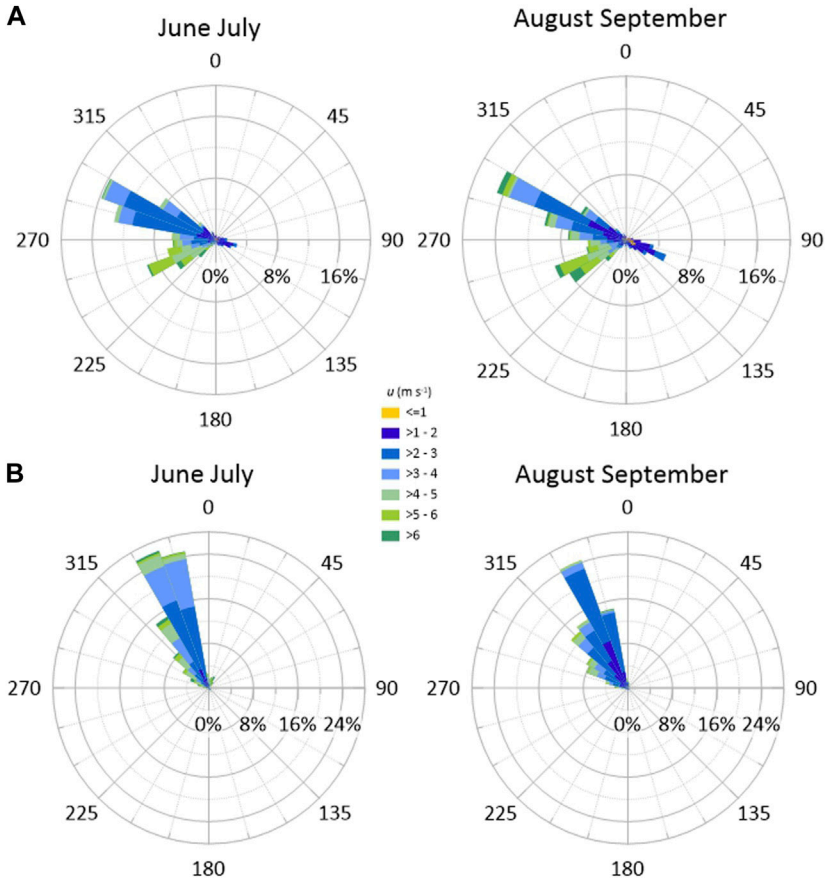

FIGURE 3
Half season wind roses for Miage Glacier at **(A)** LWS and **(B)** UWS. The radial scale shows the frequency of half hour mean winds blowing from a particular direction.

specifications can be found in that paper. Hourly precipitation totals were obtained from the Lex Blanche weather station, operated by Regione Valle d'Aosta, 4 km west of the LWS at 2,162 m a.s.l. in both 2013 and 2016. Additional hourly precipitation data were available from a rain gauge at 2,340 m a.s.l. on Miage Glacier in 2013. The incoming and outgoing longwave radiation fluxes were used to calculate debris surface temperature, T_s, using a surface emissivity of 0.94, following Brock et al. (2010). Wind speed, u (m s^{-1}), was calculated from the two horizontal wind speed components recorded by the sonic anemometer.

2.4 Surface conditions and modelling of contributing areas

To help understand processes controlling F_c recorded at the EC stations, the upwind contributing glacier surface areas, or footprints, were calculated. A particular consideration at the LWS site is the presence of forested areas 0.5–1.0 km distant which could influence F_c through photosynthesis and soil microbial processes. We calculated contributing areas using the Agroscope Reckenholz Tanikon (ART) footprint tool (Version 1.0, 13.03.2007) developed by the Swiss Federal Agricultural Research Center (Neftel et al., 2008). The ART footprint model is based on the analytical footprint model of Kormann and Meixner (2001) and has been successfully applied in the complex terrain of a debris-covered glacier (Wang and Xu, 2018).

Using analysis for all days of EC data, the glacier surface footprints at each site remain constant throughout the season and are dominated by areas <200 m from the EC stations (Figure 2). The main contributing areas are upglacier from the measurement sites corresponding with dominant wind direction (Figure 3); to the west of the LWS, with a small additional component from the south-east, and to the northwest of the UWS. The contribution of non-glacier areas was <0.1% at both sites, and hence off-glacier photosynthesis and respiration can be discounted as a significant influence on F_c recorded at the EC stations. No snow was recorded in the vicinity of the LWS during the 2013 measurement period. At the UWS, there was a continuous snow cover starting a few metres upglacier of the EC station in late June, coincident with the main contributing area. The snow cover had retreated several hundred metres upglacier by mid-July. Snow cover will therefore influence F_c at the UWS only in the first 2–3 weeks of the 2016 measurement period.

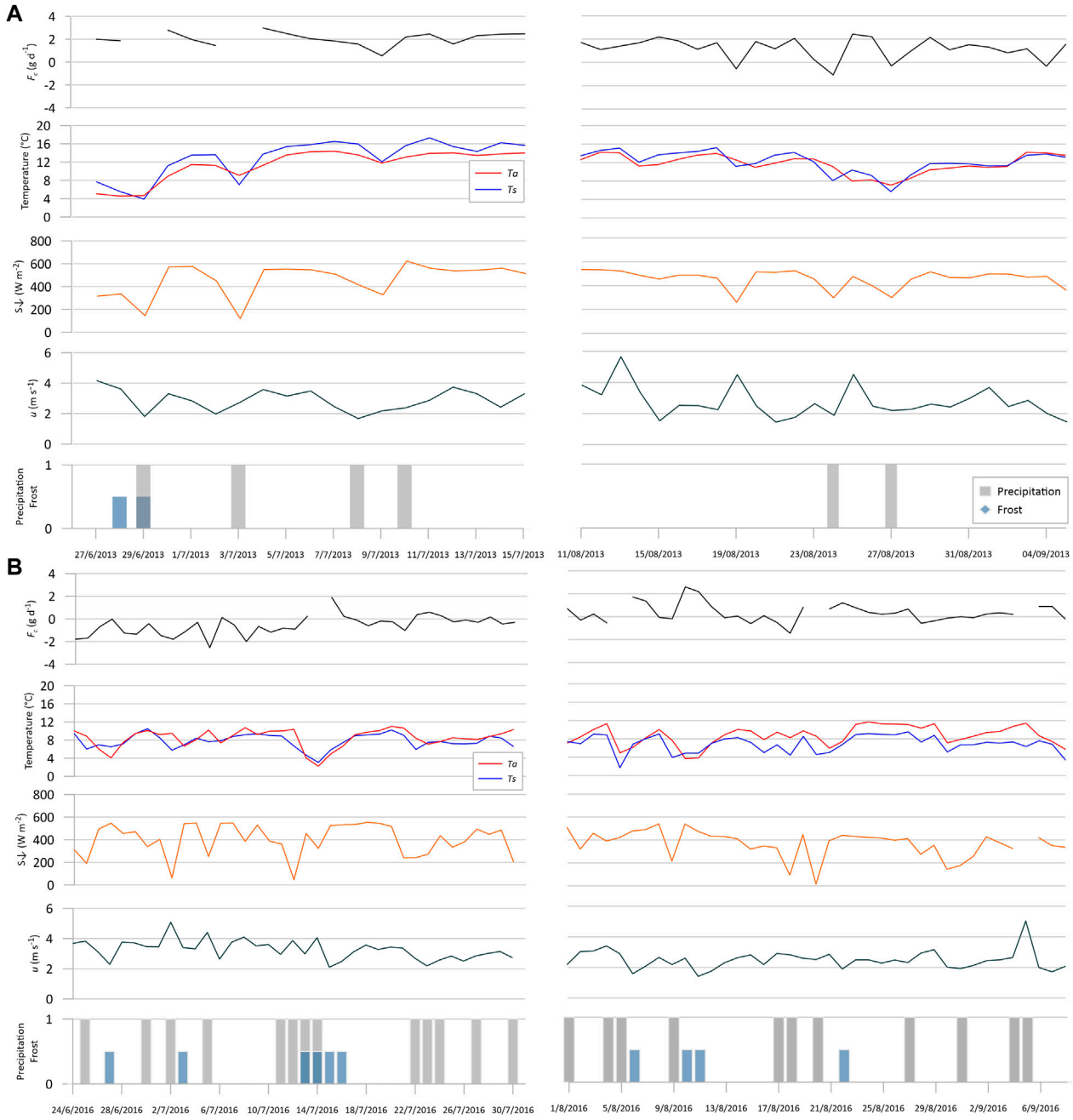

FIGURE 4
Half season daily averages of precipitation, u, $S\downarrow$, T_a, T_s, and net daily total of F_c at the **(A)** LWS in 2013, and **(B)** UWS in 2016. Precipitation and ground frost are shown as binary series, with values of 1 and 0.5 indicating days with >0.4 mm of rain (grey bars) and ground frost (blue bars), respectively. Values on 29/06 and 03/07 in 2013 and values on 14/07, 05/08, 20/08, and 05/09 in 2016 are likely to have been skewed due to a large number of missing half hour values due to rainfall, hence F_c values are not shown for these dates. The data gap at the LWS (16/07 to 10/08) was due to logger failure. Positive F_c indicate downwardly directed fluxes, and negative F_c values indicate upwardly directed fluxes.

2.5 Data analysis

In the results section, F_c is presented visually for each site as daily and half-hourly time series, and as mean daily cycles using season-averaged values for each hour of the day. Regression analysis of half hourly F_c on independent meteorological variables ($S\downarrow$, T_s, T_a, and u) is conducted on day ($S\downarrow$ >0 W m^{-2}), night ($S\downarrow$ ≤0 W m^{-2}) and half season (June-July = early season; August-September = late season) data subsets. The former subdivision is made due to the contrasting temperature regimes of debris in the day and night, and the latter subdivision is made to aid assessment of potentially influential long-term changes such as snow cover retreat, depletion of available reactive sediment within debris covers, and decline in $S\downarrow$ between the early and late season. An alpha level of 0.05 is used to identify significant relationships. As is conventional in glaciological research, in this study fluxes of energy and mass are considered positive when

directed towards the surface and negative when directed away from it.

3 Results

3.1 Seasonal trends in F_c and meteorological variables

At the LWS, daily net total F_c is positive for most days of the 2013 ablation season, with a mean of 1.58 g m^{-2} d^{-1}, indicating a net downward flux of CO_2 into the debris (Figure 4A, top trace). In the late June to mid-July period, daily total F_c varies between 1.5 and 3.0 g m^{-2} d^{-1}, except for a value of 0.6 g m^{-2} d^{-1} on 9 July. Daily net total F_c remains positive on most days from mid-August to early September, but values are slightly lower, typically in the range 0.8–2.4 g m^{-2} d^{-1}, with negative values on 19 and 24 August, and values close to zero on 23 and 27 August, and 4 September. Daily net total F_c does not exceed 2.0 g m^{-2} d^{-1} after 29 August.

F_c values at the LWS broadly correspond with the pattern of daily average $S\downarrow$, T_a, and T_s over the 2013 season, particularly in June and July (Figure 4A). Days with high positive F_c are generally concurrent with high $S\downarrow$ and T_s, indicating warm and sunny weather conditions, while low positive or negative daily F_c totals, e.g., on 9 July, and 19, 24, and 27 August, correspond with marked drops in $S\downarrow$ and T_s (Figure 4A), associated with relatively cool and cloudy conditions. There are some exceptions, e.g., daily F_c values decline between 4 and 7 July, while T_a and T_s increase, and $S\downarrow$ remains steady, over the same period, and daily F_c totals appear to be independent of $S\downarrow$, T_a, and T_s in the first week of September. There is no clear relationship between u and F_c at the LWS site, with days of high u corresponding with both high and low F_c. The days with the highest positive F_c totals in their respective half season periods: 30 June (2.8 g m^{-2} d^{-1}) and 4 July (3.0 g m^{-2} d^{-1}), and 25, 26, and 29 August (2.1–2.4 g m^{-2} d^{-1}), are preceded by days of heavy rainfall (daily totals in the range 6–33 mm) and, in most cases, very low debris surface temperatures. T_s minima were <0°C on the mornings of 28 and 29 June, and <0.5°C on the mornings of 26 and 28 August. A data gap on 25 June means the minimum for that morning is not known. However, T_s remained well above 0°C throughout 4 July, and several days in August had F_c totals >2.0 g m^{-2} in the absence of rain or very low T_s.

At the UWS site, daily total F_c totals are predominantly negative, or close to zero, in the early season June to July period, with a mean of −0.5 g m^{-2} d^{-1}, indicating a net upward flux of CO_2 from debris to the atmosphere (Figure 4B, top trace). Daily F_c totals are most strongly negative in June and the first half of July, with values in the range −2.5 to +0.2 g m^{-2} d^{-1}. In the second half of July, daily F_c totals are close to zero, ranging from −1.0 to +0.6 g m^{-2} d^{-1}, except for a notable high positive total of 1.9 g m^{-2} d^{-1} on 15 July. In contrast to the June-July period, daily F_c totals are generally slightly positive in August and September, typically ranging from −0.6 to +1.7 g m^{-2} d^{-1}, with a mean of +0.4 g m^{-2} d^{-1}, indicating a net downward flux of CO_2 to the debris in the second half of the 2016 season. There are large positive totals of 2.6 and 2.2 g m^{-2} d^{-1} on 10 and 11 August, respectively, and a large negative total of −1.4 g m^{-2} d^{-1} on 18 August. The mean daily total F_c at the UWS site over the 2016 season is −0.06 g m^{-2} d^{-1}; one-16th of its magnitude of the LWS site in 2013, and of opposite sign.

There is no clear visual relationship between daily total F_c and daily mean $S\downarrow$, T_a, T_s, and u at the UWS in the period from late June to the middle of August 2016 (Figure 4B). A weak direct relationship between daily total F_c and daily mean $S\downarrow$, T_a and T_s is apparent in the second half of August and first week of September, however, but F_c still appears to be independent of u. In similarity to the LWS, the days with the highest positive daily F_c at the UWS, in the range 1.7–2.6 g m^{-2} d^{-1} on 15 July, and 6, 10, and 11 August 2016, all occurred on days with morning T_s <0°C, following heavy rain on the previous day (Figure 4B). Meteorological conditions were similar on these days, but not unusual in comparison to the rest of 2016, with relatively high $S\downarrow$, and slightly below average T_a and T_s. Other days with morning T_s values <0°C: 27 June, 3 July, and 22 August, also show increased F_c totals compared with neighbouring days. Similarly, the 6 July, the only day in the first 3 weeks of the 2016 season with a positive F_c, total had low T_s (<0.5°C in the early morning) following heavy rain on the preceding day.

3.2 Mean daily cycle of F_c

At the LWS, hourly-averaged F_c displays a strong diurnal cycle with an approximately bell-shaped curve of positive daytime values, centred on an early afternoon peak, while the night-time F_c is characterised by negative values of smaller magnitude, with no clear relationship to the time of night (Figures 5A, 6A). On an average day in the 2013 season, the LWS F_c is positive for 12 h between 8.00 and 20.00, peaking at >90 mg m^{-2} s^{-1} (>0.3 g m^{-2} h^{-1}) between 14.00 and 15.00, while night-time F_c drops to −14 mg m^{-2} s^{-1} (−0.05 g m^{-2} h^{-1}) between 22.00 and 23.00, and then varies in a narrow range between −8 and −15 mg m^{-2} s^{-1} (approximately −0.03 to −0.05 g m^{-2} h^{-1}) until 8.00. Peak half-hour F_c exceeds 140 mg m^{-2} s^{-1} (>0.5 g m^{-2} h^{-1}) in several days in June, July, and August (Figure 5A). Both the magnitude and variability of night-time F_c increases from late June to the middle period from mid-July to mid-August, with peak half-hour F_c occasionally exceeding −50 mg m^{-2} s^{-1}, (−0.18 g m^{-2} h^{-1}) before reducing in magnitude again in late August and early September, although still with a high amount of variability (Figure 5A).

At the UWS site, hourly-averaged F_c shows a similar pattern of positive daytime, and negative night-time values, but with lower magnitude in the daytime, around one-third of that at the LWS, while night-time values are in a similar range at both sites (Figures 5B, 6B). The UWS site also shows greater temporal variability in both day and night F_c over the 2016 measurement period compared with the LWS site (Figure 5). At the UWS, F_c transitions from the early period up to the middle of July, which is dominated by relatively high negative night-time flux and weak positive daytime flux, through the second half of July when positive daytime and negative night-time fluxes are approximately in balance, to the August-September period when positive daytime fluxes generally exceed negative night-time fluxes. On an average day in the 2016 season, the UWS F_c is positive for 7 h between 10.00 and 17.00, peaking at 27 mg m^{-2} s^{-1} (~0.1 g m^{-2} h^{-1}) between 13.00 and 14.00, while night-time F_c drops to −16 mg m^{-2} s^{-1} (−0.06 g m^{-2} h^{-1}) between 20.00 and 21.00, and then gradually increases over the remainder of the night, reaching −5 mg m^{-2} s^{-1} (−0.02 g m^{-2} h^{-1}) between 8.00 and 9.00 (Figure 6B). Daytime, half-hour F_c rarely exceeds 60 mg m^{-2} s^{-1}, (~0.2 g m^{-2} h^{-1}) but peak fluxes over 110 mg m^{-2} s^{-1} (~0.4 g m^{-2} h^{-1}) are recorded on 3 days, all of which had morning T_s <0°C (Figure 5B).

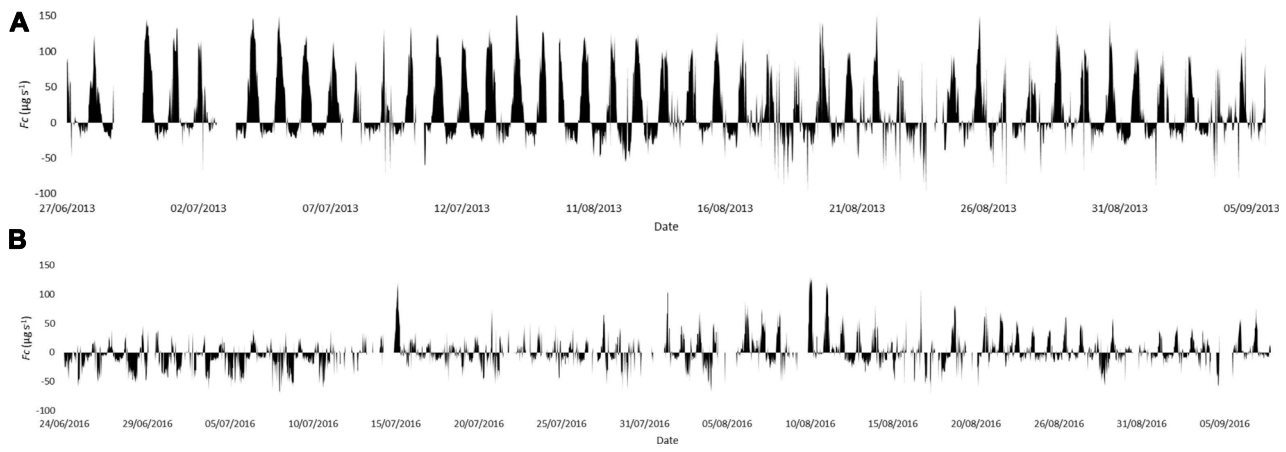

FIGURE 5
Time series of half hourly F_c at the: **(A)** LWS and **(B)** UWS throughout the monitoring period.

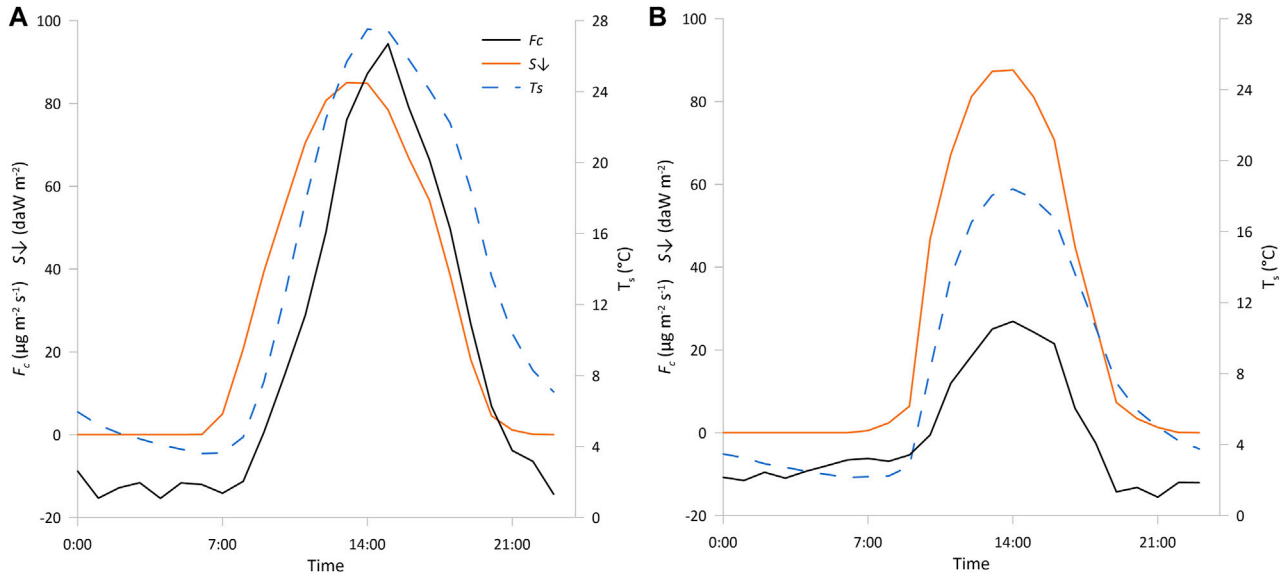

FIGURE 6
Daily average cycles of F_c, $S\downarrow$, T_s at the **(A)** LWS and **(B)** UWS. Downwards directed F_c are represented by positive values and upwards directed F_c by negative values.

3.3 Relationship between mean daily cycles of F_c, T_s, and $S\downarrow$

There is a striking similarity in the form and temporal alignment of the mean daytime cycles of F_c, T_s, and $S\downarrow$ at both sites (Figures 6A, B). At the LWS site, the initial morning rise and daytime peak of $S\downarrow$ occur 1 hour earlier than the corresponding inflection points in the F_c curve, whereas T_s and F_c vary in unison, with temporally aligned inflection points in the morning, early afternoon, and evening. At the UWS site, the initial morning rise in $S\downarrow$ occurs 1 hour earlier than the corresponding rises in F_c and T_s, however, the peak values of all 3 variables occur together between 13.00 and 14.00, and their evening inflection points are similarly temporally aligned. While $S\downarrow$ is of similar magnitude at the LWS and UWS in the 10.00–17.00 high flux period, with mean values of 747 and 743 W m^{-2}, respectively, F_c and T_s values over the same period are much lower at the UWS, at 28% and 67% of their LWS values, respectively. The duration of high $S\downarrow$ values over 100 W m^{-2} is 3 h shorter at the UWS compared with the LWS due to topographic shading in the early morning and evening. During the night, hourly mean T_s gradually decreases from the late evening to a minimum value between 5.00 and 6.00 at both sites, while over the same period F_c contrasts between a gradual and variable increasing trend at the UWS, and no trend with small variability at the LWS.

TABLE 2 Regression analysis of F_c (half hourly values) on meteorological variables. F_c in mg m^{-2} s^{-1}; T_s and T_a in °C, u in m^{-2} s^{-1} and $S\downarrow$ in W m^{-2}. Shaded rows indicate night analyses and clear rows indicate day analyses. Significant relationships are denoted by bold values ($p \leq 0.05$).

Predictors	LWS full season 2013 (day n = 1,166; night n = 775)			UWS full season 2016 (day n = 1794; night n = 1,134)		
	Coef	SE Coef	R^2	Coef	SE Coef	R^2
T_s	**3.86**	**0.10**	**0.57**	**2.21**	**0.0828**	**0.28**
	0.39	0.23	0.00	**−3.98**	**0.232**	**0.21**
T_a	**6.72**	**0.33**	**0.27**	**1.49**	**0.213**	**0.03**
	0.00	0.26	0.00	**−2.98**	**0.180**	**0.20**
u	**10.61**	**0.74**	**0.15**	**−8.27**	**0.510**	**0.12**
	−4.64	**0.54**	**0.09**	**−11.42**	**0.392**	**0.43**
$S\downarrow$	**0.0973**	**0.0030**	**0.47**	**0.0399**	**0.0014**	**0.33**
	June—July 2013 (day n = 484; night n = 256)			June—July 2016 (day n = 919; night n = 496)		
T_s	**4.0892**	**0.1427**	**0.63**	**1.41**	**0.11**	**0.15**
	−0.3023	0.2223	0.00	**−3.70**	**0.36**	**0.18**
T_a	**6.3714**	**0.4787**	**0.27**	**−1.04**	**0.28**	**0.01**
	−0.48	**0.2024**	**0.02**	**−3.24**	**0.29**	**0.20**
u	**15.3307**	**1.192**	**0.25**	**−8.95**	**0.57**	**0.21**
	−6.1242	**0.6859**	**0.24**	**−11.92**	**0.57**	**0.46**
$S\downarrow$	**0.1120**	**0.0034**	**0.69**	**0.0283**	**0.0017**	**0.24**
	August—September 2013 (day n = 682; night n = 519)			August—September 2016 (day n = 875; night n = 638)		
T_s	**3.67**	**0.14**	**0.51**	**2.95**	**0.10**	**0.48**
	0.59	0.31	0.05	**−4.07**	**0.30**	**0.22**
T_a	**6.97**	**0.45**	**0.26**	**2.69**	**0.30**	**0.09**
	0.26	0.39	0.00	**−2.74**	**0.22**	**0.19**
u	**7.96**	**0.93**	**0.10**	**−3.36**	**0.98**	**0.01**
	−4.34	**0.69**	**0.07**	**−12.17**	**0.62**	**0.38**
$S\downarrow$	**0.0823**	**0.0047**	**0.31**	**0.0563**	**0.0017**	**0.55**

3.4 Statistical analysis of the relationship of F_c to meteorological variables

Results of the statistical analysis are presented in Tables 2, 3; Figures 7, 8.

Daytime F_c has significant direct relationships to T_s, and $S\downarrow$ at both the LWS and UWS sites and in both half-season and full season data sets. The simple linear regression relationships are strongest at the LWS, particularly in the June-July period when T_s, and $S\downarrow$ each account for >60% of the variance in daytime F_c, with the slight lag between daytime cycles of F_c and independent variables (Figure 6) and associated hysteresis accounting for some of the unexplained variance. The relationships of F_c to T_s, and $S\downarrow$ at the UWS are weak, although significant, in the June-July period but become much stronger in August-September when $S\downarrow$ explains a greater amount of F_c variance than at the LWS. The slope coefficients for the regressions of F_c on T_s, and $S\downarrow$ at the LWS decrease between June-July and August-September indicating a lower sensitivity of F_c

TABLE 3 Correlation matrix of F_c and environmental variables. All correlations are significant at $p \leq 0.05$.

LWS				
	F_c	T_s	T_a	$S\downarrow$
T_s	0.718			
T_a	0.504	0.852		
$S\downarrow$	0.692	0.756	0.517	
u	0.336	0.335	0.277	0.116
UWS				
T_s	0.496			
T_a	0.120	0.702		
$S\downarrow$	0.573	0.915	0.369	
u	−0.377	0.141	0.371	−0.035

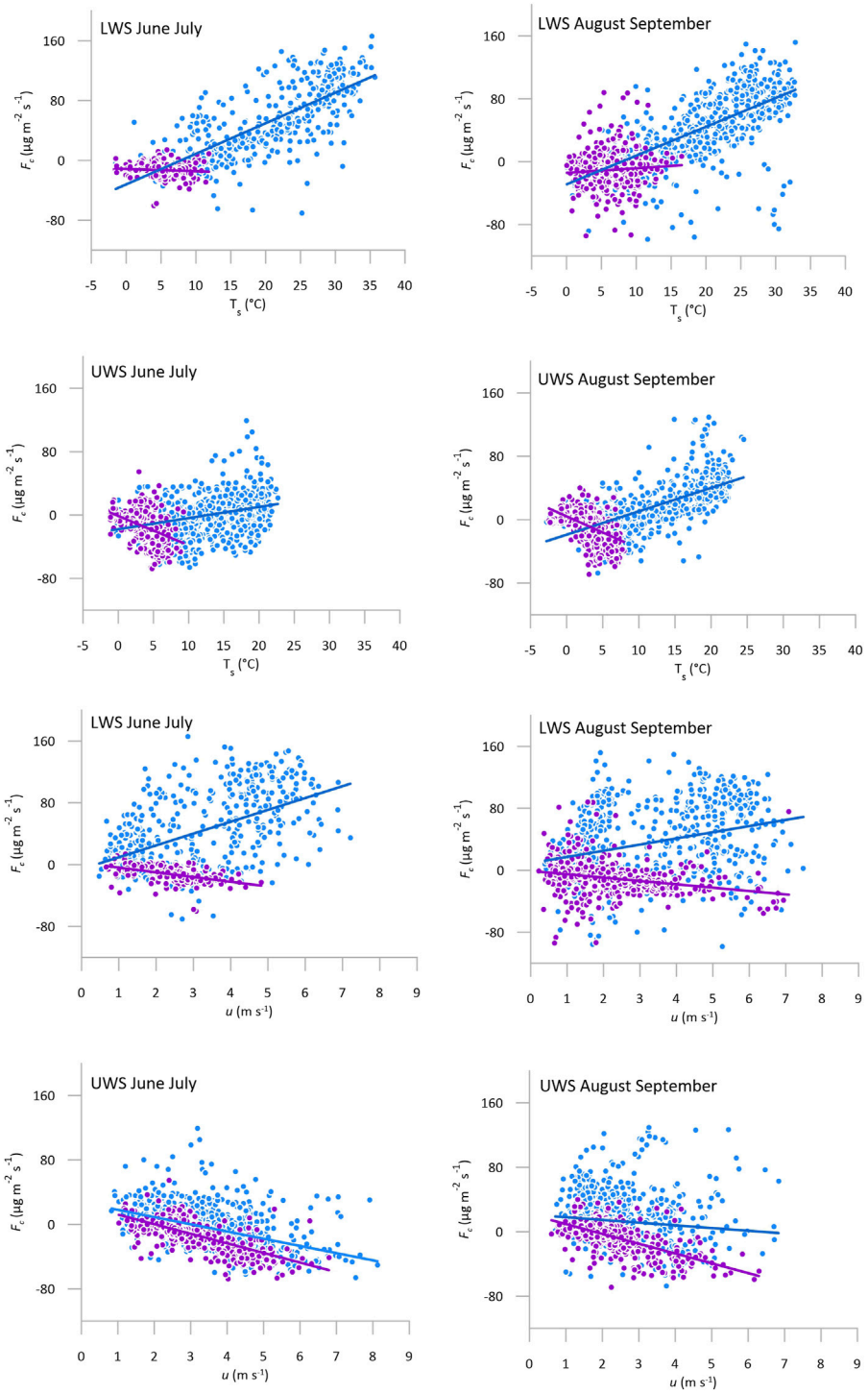

FIGURE 7
Relationships of F_c to surface temperature (T_s, top four plots) and wind speed (u, bottom four plots) at: the LWS (rows 1 and 3) and UWS (rows 2 and 4) in June-July (left column) and August-September (right column). Daytime and night-time half hourly mean values are shown by the blue and purple circles, respectively, together with best linear least squares regressions (blue and purple lines). Downwards directed F_c is represented by positive values and upwards directed F_c by negative values.

to debris surface temperature and incoming shortwave radiation in the second half of the season. In contrast, at the UWS the corresponding slope coefficients increase between June-July and August-September, approximately doubling the sensitivity of F_c to T_s, and $S\downarrow$ in the second half of the season, although still with lower sensitivity than at the LWS. The scatter of high magnitude negative

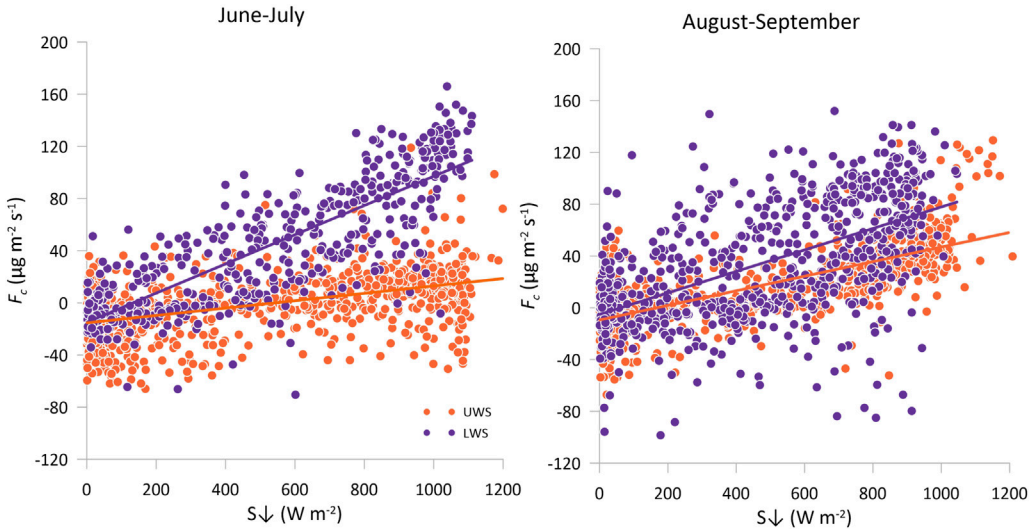

FIGURE 8
June-July and August-September relationship of F_c to incoming shortwave radiation (S↓). LWS and UWS values are shown by purple and orange circles, respectively, together with best fit linear least squares repressions (purple and orange lines). Downwards directed F_c is represented by positive values and upwards directed F_c by negative values.

daytime F_c values, visible in the LWS graphs, particularly in August-September (Figure 7 top two panels and Figure 8), is mostly associated with rainfall events when it is possible that water interfered with gas analyser measurements, even though the instrument signal strength was above threshold. Hence, the decrease in slope coefficients and R^2 values between June-July and August-September for the relationships of F_c to T_s, and $S\downarrow$ at the LWS may be at least partly due measurement error, rather than purely due to change in physical process.

Daytime F_c has significant direct relationships to T_a and u at the LWS, with the slope coefficient and R^2 value for the T_a relationships quite consistent between June-July and August-September but dropping markedly for the u relationships over the same period (Table 2). In contrast, daytime F_c has a weak, although significant, dependency on T_a at the UWS, changing from an inverse to a direct relationship between June-July and August-September. The relationship of daytime F_c to u at the UWS is significant and inverse in both periods, changing from a moderately strong relationship in June-July to a very weak relationship in August-September. The night-time relationships of F_c to T_s and T_a at the LWS are either weak or non-significant, but F_c has a moderately strong and significant inverse night-time relationship to u in June-July, becoming weak, although still significant, in August-September (Table 2; Figure 7). In contrast, at the UWS night-time F_c has moderately strong and significant inverse relationships to T_s, T_a, and u in both June-July and August-September. In particular, u accounts for almost half of night-time F_c variance at the UWS in June-July, and over a third in August-September.

A stepwise regression procedure was used to develop multivariable relationships to explain F_c variance, whilst accounting for collinearity between independent variables, with the resulting significant relationships for F_c in mg m^{-2} s^{-1} as follows:

LWS daytime:

$$Full\ season\text{: } F_c = -6.7 + 4.6T_s - 5.42T_a + 0.0303S\downarrow + 6.1u, R^2 = 0.69. \quad (1)$$

$$Jun-Jul\text{: } F_c = -23.3 + 3.17T_s - 3.4T_a + 8.0u + 0.0533S\downarrow, R^2 = 0.805. \quad (2)$$

$$Aug-Sep\text{: } F_c = 7.2 + 5.22T_s - 6.69T_a + 0.0177S\downarrow + 5.1u, R^2 = 0.608. \quad (3)$$

UWS daytime:

$$Full\ season\text{: } F_c = 8.3 + 0.0251S\downarrow + 0.9T_s - 8.1u, R^2 = 0.477. \quad (4)$$

$$Jun-Jul\text{: } F_c = 15.4 + 0.0278S\downarrow - 8.1u - 0.38T_a, R^2 = 0.433. \quad (5)$$

$$Aug-Sep\text{: } F_c = 11.5 + 4.82T_s - 5.3T_a + 1.4u, R^2 = 0.605. \quad (6)$$

LWS night-time:

$$Full\ season\text{: } F_c = 8.8 - 4.9u + 2.23T_s - 2.13T_a, R^2 = 0.111. \quad (7)$$

$$Jun-Jul\text{: } F_c = 7.4 - 6.17u - 0.52T_a, R^2 = 0.258. \quad (8)$$

$$Aug-Sep\text{: } F_c = 8.9 - 4.8u + 2.5T_s - 2.28T_a, R^2 = 0.097. \quad (9)$$

UWS night-time:

$$Full\ season\text{: } F_c = 23.5 - 10.4u - 0.69T_a, R^2 = 0.435. \quad (10)$$

$$Jun-Jul\text{: } F_c = 25.6 - 11.3u - 0.45T_a, R^2 = 0.468. \quad (11)$$

$$Aug-Sep\text{: } F_c = 23.4 - 10.9u - 0.65T_a, R^2 = 0.385. \quad (12)$$

All four meteorological variables (T_s, T_a, $S\downarrow$ and u) independently explain part of the daytime F_c variance at the LWS, with T_s accounting for the largest portion, and $S\downarrow$ and u the least, and these relationships have very high coefficients of determination, particularly in June-July (Eqs 1–3). F_c sensitivity to T_s and T_a increases between June-July and August-September but

decreases for $S\downarrow$ and u. Interestingly, the T_a slope coefficient reverses from a positive value in the simple linear regressions (Table 2) to a negative value in the multiple regression relationships (Eqs 1–3). This implies that the apparent positive relationship of F_c to T_a in the simple linear regressions is most likely spurious and due to the strong positive correlation of T_a with T_s and $S\downarrow$ (Table 3). The UWS June-July daytime multiple regression relationship (Eq. 5) has a lower R^2 and a different form to the LWS daytime relationships (Eqs 1–3), with F_c most strongly dependent on $S\downarrow$, independent of T_s, weakly dependent on T_a, and with an inverse relationship to u. In contrast, the UWS August-September daytime multiple regression relationship and coefficient of determination (Eq. 6) are similar to the August-September daytime LWS relationship (Eq. 3), except that F_c at the UWS is independent of $S\downarrow$.

The LWS night-time multiple regression relationships account for only a small proportion of F_c variance, almost entirely associated with the inverse relationship of F_c flux to u, despite the inclusion of T_s and T_a as independent variables (Eqs 7–9). By comparison, the UWS night-time relationships have higher coefficients of determination, particularly in June-July, which again is almost entirely dependent on the inverse relationship of F_c flux to u, with T_a accounting for only a small part of F_c variance (Eqs 10–12).

4 Discussion

4.1 F_c magnitude on debris covered glaciers

The seasonal F_c values infer that thick supraglacial debris is a net CO_2 sink over the ablation period, while on thin supraglacial debris net CO_2 exchange is close to zero. Assuming the LWC EC measurements are representative for thick debris generally, the mean downward flux of 1.58 g m^{-2} d^{-1} would equate to 1.58 t CO_2 km^{-2} d^{-1}. With thick debris extending well over 3 km^2 over the glacier's surface (Mihalcea et al., 2008; Foster et al., 2012) total drawdown over a 100-day ablation season (a conservative estimate for Miage glacier; Brock et al., 2010) could be of the order of 500 t CO_2 (0.5 Gg CO_2). In units of carbon, the total ablation season drawdown for the thick debris area at Miage Glacier would be ~43 t C km^{-2}. For comparison, this is 4 times the very high drawdown rate estimated for marginal surface areas of the Greenland Ice Sheet associated with CO_2 consumption by photoautotrophic algae (Cook et al., 2012).

EC measurements of F_c over supraglacial debris are rare. To our knowledge, the only other comparable study is that of Wang and Xu (2018), who reported a net downwardly oriented F_c of 58.68 mmol m^{-2} d^{-1} (equivalent to 2.58 g m^{-2} d^{-1}) over 2 years of EC measurements at Koxkar Glacier, western Tien Shan. The Koxkar Glacier site was at higher elevation (3,212 m) and on thicker debris (0.72 m) than the Miage glacier sites and included measurements during the winter accumulation and spring snow melt periods, as well as the summer ablation season. However, the magnitude of F_c is similar at both glaciers, and this strongly suggests that debris-covered glaciers with extensive covers of thick cover of silicate rocks are important to local and regional carbon cycling. Without data from outside of the ablation season, the net annual F_c at Miage glacier cannot be determined, although the small number of measurements at T_s<0°C suggest F_c magnitude becomes very small at negative temperatures. Wang and Xu (2018) observed that low rates of CO_2 drawdown continued in winter at Koxkar Glacier, even when debris was snow covered and melting absent.

TABLE 4 Seasonal averages of environmental variables.

	T_s (°C)	T_a (°C)	$S\downarrow$ (W m^{-2})	u (m s^{-1})
LWS June July	12.9	11.4	459.4	2.9
LWS August September	12.3	11.8	457.7	2.8
UWS June July	7.9	8.5	405.9	3.3
UWS August September	7.2	8.8	373.6	2.5

4.2 Processes controlling F_c magnitude and direction

The high magnitude daytime downward F_c at the LWS site, and at the UWS site in the mid July to early September period, is most likely due to CO_2 drawdown induced by a combination of hydrolysis and carbonation reactions. During the day, the debris is warmed by solar radiation, and heat energy is conducted downwards through the debris layer leading to melting of ice at the debris interface (Reid and Brock, 2010). The rates of both diffusion of atmospheric CO_2 into meltwater and rock chemical weathering will increase when T_s increases, because: i) the supply of fresh low $p(CO_2)$ meltwater is greatest when debris surface temperature is highest; and ii) the rate of chemical reaction increases with temperature (Arrhenius principle). These interlinked processes generate a daytime F_c cycle which corresponds closely with, but slightly lags, the daytime cycles of $S\downarrow$ and T_s (Figure 6). Fyffe et al. (2019b) established that surface meltwater at Miage Glacier flows through debris and drains into supraglacial streams, and so water in the debris matrix could be replenished by new ice melt before it becomes saturated in dissolved CO_2. The combination of the melt-driven supply of fresh dilute water, high temperatures, and reactive mineral surfaces open to the atmosphere makes supraglacial debris an ideal environment for rock chemical weathering and consumption of atmospheric CO_2 during the ablation season. With these conditions, daytime CO_2 drawdown rates can exceed 0.5 g m^{-2} h^{-1} when T_s exceeds 30°C, but approach zero when $T_s \leq$0°C (Figure 7). $S\downarrow$ and daytime T_s both correlate strongly with F_c (Table 2) but this consideration of processes, and the lag between increasing $S\downarrow$ and F_c in the morning (Figure 6), points to a primary role for insolation in providing energy to heat debris and drive melting, rather than being a direct control on F_c. Similarly, daytime T_a and u correlate with F_c primary because their daily cycles are controlled to a great extent by T_s (Brock et al., 2010).

The strong relationship of F_c to T_s and $S\downarrow$ is consistent between the early and late season at the LWS, and late season at the UWS (Table 2; Eqs 2, 3, 6; Figures 7, 8). The early season period at the UWS is distinct, however, with F_c only weakly dependent on $S\downarrow$ and T_s (Table 2; Eq. 5; Figures 7, 8), and of much lower daytime magnitude, particularly in the first 3 weeks, than in the remainder of the 2016 season (Figure 4B, upper trace). This

cannot be explained by changing meteorological conditions because T_s, T_a, $S\downarrow$, and u are very similar between the early and late ablation season (Table 4). The most likely explanation is the presence of extensive snow cover in the area upwind from the UWS in the early part of the 2016 ablation season. Trace gases can diffuse through seasonal snow cover (e.g., Seok et al., 2009) so the likely control of snow cover on F_c is the inhibition of processes of CO_2 uptake in debris. The high albedo and low thermal conductivity of snow will strongly reduce the heat flux to the underlying debris, suppressing ice melt and rock weathering, and limiting the consumption of atmospheric CO_2 through carbonation. The UWS site itself was already snow free when the EC station was installed, enabling the debris there to warm in response to daytime insolation. Hence, there would have been a mismatch between the sample area of $S\downarrow$ and T_s, unaffected by snow cover at, or close to, the UWS site, and the snow-covered CO_2 footprint area extending 200 m upglacier, resulting in weak relationships of F_c to $S\downarrow$ and T_s. Over time, the snow cover retreated, gradually increasing the area of exposed debris in the UWS contributing area. The 4-day rain event from 11 to 14 July 2016 (Figure 4B) likely removed most of the remaining snow cover within 200 m of the UWS, and subsequently daytime F_c magnitude increased (Figure 5B) and daily F_c totals transitioned from strongly negative to close to zero (Figure 4B).

Two pieces of evidence imply that the rate of daytime CO_2 drawdown is sediment limited. First, the sensitivity of daytime F_c to T_s is lower at the thin debris UWS site compared to the thick debris LWS site (Table 2; Figure 7) and F_c is greater at the LWS than the UWS for the same debris surface temperatures at all values of $T_s > 8^{\circ}C$. Meltwater supply rate cannot be the reason for lower daytime F_c at the UWS since ice melt rates would generally be higher at the UWS due to the lower thermal resistance of thin debris cover (Reid and Brock, 2010; Fyffe et al., 2014). The likely explanation for lower F_c at the UWS is the smaller debris-water contact area in the 0.04 m debris layer, compared with the 0.23 m layer at the LWS, resulting in a lower rate of hydrolysis and atmospheric CO_2 drawdown.

Second, daily total F_c is higher on days following rain-debris frost events. At the UWS, daily F_c totals on 15 July and 6, 7, 10, and 11 August 2016 are >1.5 g m^{-2} d^{-1}, much higher than the mean daily UWS flux of −0.06 g m^{-2} d^{-1} and comparable to the mean daily F_c total at the LWS of 1.58 g m^{-2} d^{-1} (Figure 4). Similarly, the second highest daily F_c total at the LWS occurred on 30 June following a rain-debris frost event (Figure 4). These results implicate the role of frost shattering in supplying comminuted reactive sediment for chemical reactions in the debris layer, particularly in thin debris covers. Freshly exposed mineral surfaces are highly reactive in contact with water (St Pierre et al., 2019; Wadham et al., 2019) and would be rapidly chemically weathered with the onset of debris warming and ice melt in the day following the frost, in turn leading to a transitory acceleration in atmospheric CO_2 drawdown. Saturation of rocks by rain followed by sub-zero temperatures, as occurred in the debris frost events identified (Figure 4), creates ideal conditions for mechanical fracture of rock clasts, due to the stress applied by expansion of freezing water in pores and along grain boundaries (Matsuoka, 1990). During fieldwork, recently shattered clasts were frequently observed on and in the debris cover, particularly in the higher parts of the debris-covered zone. There were some days at the LWS site when daily total F_c exceeded 2 g m^{-2} d^{-1} without preceding rain or frost, suggesting the availability of recently shattered sediment is less of a control on CO_2 drawdown rate in areas of thick debris. It is possible, however, that alluviation of shattered sediment by rain at the LWS on the 3 July 2013 supplied fresh reactive material to the lower water-saturated horizon of the debris layer, leading to the highest daily F_c total on 4 July. At the UWS, increases in F_c following debris frosts on 27 June and 3 July 2016 were of likely of small magnitude due to widespread snow cover at the time.

Night F_c is predominantly negative with similar magnitude at both sites: LWS night mean = −41 mg m^{-2} h^{-1} and UWS night mean = −35 mg m^{-2} h^{-1}. The flux of CO_2 to the atmosphere in the night is most likely due to respiration by debris-dwelling microorganisms dominating net surface CO_2 exchange while hydrolysis and carbonation rates are low. Microbially-mediated sulphide oxidation, if present, could generate high p (CO_2) in immobile pore waters located above the night-time water table, potentially adding to night-time CO_2 emission. It is also possible that expulsion of dissolved CO_2 during overnight freezing of water in the debris periodically contributes to the negative night-time F_c. In the daytime at low T_s, F_c is also negative and of similar magnitude to the night-time, for example, for $T_s < 6^{\circ}C$, daytime mean F_c is −32 mg m^{-2} h^{-1} at the LWS and −27 mg m^{-2} h^{-1} at the UWS. Hence, microbial respiration is not restricted to night-time, but its impact on net F_c in the daytime is normally masked by the much higher magnitude of CO_2 consumption by hydrochemical reactions.

A noticeable difference between the two sites is that night-time F_c at the LWS is independent of T_s and T_a, and only weakly dependent on u, whereas at the UWS night-time F_c is significantly inversely dependent on all three independent variables (Table 2; Figure 7). The apparent relationship of night-time F_c to u, T_s and T_a at the UWS is likely to be spurious, however, because all four variables depend strongly on time of the night, with seasonally averaged hourly values decreasing almost monotonically from 8 p.m. to 8 a.m. For example, hourly averaged F_c and u correlate more strongly with hour since 7 p.m. (Pearson's r values = 0.955 and 0.944, respectively) than they do with each other (Pearson's $r = 0.882$). An alternative explanation for the night-time trend of decreasing F_c at the UWS lies in the differing water retention between thick and thin debris layers. Daytime meltwater would be expected to drain quickly from the thin debris layer at the UWS but be partly retained within thick debris at the LWS (Fyffe et al., 2019b). Heterotrophic activity in soils is known to be moisture limited (Manzoni et al., 2012). Hence, the decreasing magnitude of F_c over the course of the night at the UWS might be due to decreasing water availability limiting microbial activity, while water availability is not a restrictive factor at the LWS (Figure 6). In this context, the diurnal cycle of F_c (Figure 6) can be at least partly explained through the dynamics of the debris water table, with daytime flooding and night-time drainage of meltwater varying the mixing ratio of mobile low $p(CO_2)$ meltwater to immobile high $p(CO_2)$ porewater dominated by microbial respiration. Differences in respiration rate between the UWS and LWS might also relate to spatial variation in microbial

communities on DCGs, which have been observed to increase in complexity and become increasingly heterotrophic downglacier, with increasing debris thickness and age (Franzetti et al., 2013; Darcy et al., 2017). At the UWS site, net release of CO_2 during the early season (Figure 5B) suggests microbial respiration may be important during the late winter and early ablation period of snow cover retreat.

5 Conclusion

We have presented an analysis of near-surface atmospheric CO_2 flux and its relationship to meteorological and environmental variables at contrasting thick and thin debris sites on an alpine debris-covered glacier over two ablation seasons, using eddy covariance measurements. The main conclusions are.

1. Miage glacier is a net sink of CO_2 over the ablation season. The mean drawdown rate over a thick 0.23 m debris layer, typical of most of the debris-covered zone, was 1.58 g m^{-2} d^{-1} which, if spatially representative, implies a drawdown rate of >150 t CO_2 km^{-2} over an ablation season, and over 500 t CO_2 (0.5 Gg CO_2), for the whole Miage glacier debris-covered zone. This rate is substantially higher than rates of CO_2 uptake by photosynthesising microorganisms on the surface of the Greenland Ice Sheet (Cook et al., 2012) but similar to the rate measured on a thick debris layer at Koxkar Glacier, Tianshan Mountains, China (Wang and Xu, 2018).
2. The ablation season mean CO_2 flux over a higher-elevation thin debris site, with mean thickness 0.04 m, was close to net zero, with a net rate of CO_2 release to the atmosphere of 0.06 g m^2 d^1. This included an early period of snow cover, dominated by an upward flux of CO_2 (mean flux = −0.5 g m^2 d^1). The net flux reversed sign following melting of the snow and the August-September period was dominated by net drawdown of CO_2, albeit at a lower rate (mean flux = 0.4 g m^2 d^1) than at the lower thick debris site.
3. The high rate of drawdown is likely due to dissolution of CO_2 in carbonation and hydrolysis reactions in wet debris layers. The combination of the melt-driven supply of fresh low $p(CO_2)$ water, high temperatures, and reactive mineral surfaces open to the atmosphere makes supraglacial debris an ideal environment for rock chemical weathering and consumption of atmospheric CO_2 during the ablation season.
4. Mean CO_2 flux alternates between downward and upward orientation in the day and night, respectively, and the night-time flux is around one-third of the daytime flux magnitude. The daytime flux has a pronounced curve, with the drawdown rate closely correlated with the cycle of debris surface temperature, peaking in the early afternoon. Solar radiation is an important driver in heating the debris layer, providing heat energy for ice melt and chemical weathering reactions; and CO_2 flux is low on overcast days.
5. Net CO_2 release to the atmosphere in the night, and in the daytime when debris surface temperature is below 7°C, is most likely due to respiration by microorganisms. Biological respiration almost certainly continues during the day, but only dominates the net CO_2 flux at low temperatures when chemical weathering rates are low. Decreasing meltwater availability with time overnight may be a limiting factor on microbial activity in thin debris.
6. CO_2 drawdown rates are controlled by the supply of fresh mineral surfaces and water, particularly on thin debris. On days following rainfall-debris frost events, daytime CO_2 drawdown increased by an order of magnitude to a rate comparable to thick debris. Frost shattering of saturated debris during overnight freezing likely provides abundant fresh reactive sediment which is rapidly chemically weathered with the onset of ice melting the following day. An increase in daytime CO_2 drawdown rate of lower magnitude was also observed following a debris frost event at the thick debris site.

Our results imply that debris-covered glaciers are important to local and regional carbon cycling, and further measurement of CO_2 fluxes over supraglacial debris, and research into driving processes is warranted, considering the large and growing global extent of global supraglacial debris (Scherler et al., 2018; Herreid and Pellicciotti, 2020; Tielidze et al., 2020). Future studies should encompass different geological and climatic regions and involve geochemical analyses of rocks and meltwater to establish key hydrolysis reactions and the long-term fate of carbon exported as glacier runoff. Monitoring of temperature, pH, conductivity and $p(CO_2)$ of water in the debris layer, in conjunction with isotopic analyses to identify the source of carbon in runoff, could prove to be particularly insightful. Very few studies have investigated the microecology of debris covered glaciers, and more research, including DNA sequencing of debris rock/soil samples and taxonomic ecology, is needed to identify species and their functional roles in carbon cycling. Eddy covariance is found to be a suitable tool for monitoring the near-surface CO_2 flux at short- and long-term timescales, but uncertainties in eddy covariance flux measurements and their interpretation at glacier sites (*e.g.*, Nicholson and Stiperski, 2020) and its restriction to a small number of measurements sites, could be addressed though distributed sampling of CO_2 fluxes, *e.g.*, using portable gas analysers. These studies should lead to the development of a model for CO_2 exchange in supraglacial debris that could be used to test understanding of key processes and provide estimates of fluxes at regional and global scales.

Data availability statement

The raw data supporting the conclusion of this article will be made available by the authors, without undue reservation.

Author contributions

BB conceived the study and led the data collection. GB led the data analysis and prepared the figures. All authors contributed to the article and approved the submitted version.

Funding

GB is supported by a UK Natural Environment Research Council (NERC) studentship (NE/S007512/1). Article processing charges were paid by the Northumbria University UKRI block grant.

Acknowledgments

We gratefully acknowledge provision of scientific equipment and support for fieldwork costs by Northumbria University. We give our thanks to Catriona Fyffe (Institute of Science and Technology, Austria), Mike Lim (Northumbria University, United Kingdom), Thomas Shaw (Swiss Federal Institute, WSL, Switzerland), Matt Westoby (University of Plymouth, United Kingdom) for help with glacier fieldwork, and Jean-Pierre Fosson, Marco Vagliasindi (Fondazione Montagna Sicura, Courmayeur, Italy), Edoardo Cremonese, Fabrizio Diotri (Agenzia Regionale per la Protezione dell'Ambiente Valle d'Aosta, Italy), and Philip Deline (Universite Savoie Mont Blanc, France) for fieldwork logistical support. We also thank two reviewers and Editor Xin Wang for their constructive comments on the manuscript.

Conflict of interest

The authors declare that the research was conducted in the absence of any commercial or financial relationships that could be construed as a potential conflict of interest.

Publisher's note

All claims expressed in this article are solely those of the authors and do not necessarily represent those of their affiliated organizations, or those of the publisher, the editors and the reviewers. Any product that may be evaluated in this article, or claim that may be made by its manufacturer, is not guaranteed or endorsed by the publisher.

References

Anesio, A. M., Hodson, A. J., Fritz, A., Psenner, R., and Sattler, B. (2009). High microbial activity on glaciers: Importance to the global carbon cycle. *Glob. Change Biol.* 15 (4), 955–960. doi:10.1111/j.1365-2486.2008.01758.x

Anesio, A., Sattler, B., Foreman, C., Telling, J., Hodson, A., Tranter, M., et al. (2010). Carbon fluxes through bacterial communities on glacier surfaces. *Ann. Glaciol.* 51 (56), 32–40. doi:10.3189/172756411795932092

Azzoni, R. S., Franzetti, A., Fontaneto, D., Zullini, A., and Ambrosini, R. (2015). Nematodes and rotifers on two Alpine debris-covered glaciers. *Ital. J. Zool.* 82 (4), 616–623. doi:10.1080/11250003.2015.1080312

Baldocchi, D. D. (2019). How eddy covariance flux measurements have contributed to our understanding of Global Change Biology. *Glob. Change Biol.* 26, 242–260. doi:10.1111/gcb.14807

Benn, D. I., Bolch, T., Hands, K., Gulley, K., Luckman, A., Nicholson, L. I., et al. (2012). Response of debris-covered glaciers in the Mount Everest region to recent warming, and implications for outburst flood hazards. *Earth-Sci. Rev.* 114, 156–174. doi:10.1016/j.earscirev.2012.03.008

Benn, D. I., and Evans, D. J. A. (2010). *Glaciers and glaciation*. 2nd ed. London: Hodder Arnold.

Benn, D. I., Thompson, S., Gulley, J., Mertes, J., Luckman, A., and Nicholson, L. (2017). Structure and evolution of the drainage system of a Himalayan debris-covered glacier, and its relationship with patterns of mass loss. *Cryosphere* 11 (5), 2247–2264. doi:10.5194/tc-11-2247-2017

Brock, B. W., Mihalcea, C., Kirkbride, M. P., Diolaiuti, G., Cutler, M. E., and Smiraglia, C. (2010). Meteorology and surface energy fluxes in the 2005–2007 ablation seasons at the Miage debris-covered glacier, Mont Blanc Massif, Italian Alps. *J. Geophys. Res. Atmos.* 115 (D9), D09106. doi:10.1029/2009JD013224

Brown, G. H. (2002). Glacier meltwater hydrochemistry. *App. Geochem.* 17 (7), 855–883. doi:10.1016/S0883-2927(01)00123-8

Caccianiga, M., Andreis, C., Diolaiuiti, G., D'Agata, C., Mihalcea, C., and Smiraglia, C. (2011). Alpine debris-covered glaciers as a habitat for plant life. *Holocene* 21 (6), 2011–1020. doi:10.1177/0950683611400219

Collier, E., Nicholson, L. K., Brock, B. W., Maussion, F., Essery, R., and Bush, A. B. G. (2014). Representing moisture fluxes and phase changes in glacier debris cover using a reservoir approach. *Cryosphere* 8, 1429–1444. doi:10.5194/tc-8-1429-2014

Cook, J. M., Hodson, A. J., Anesio, A. M., Hanna, E., Yallop, M., Stibal, M., et al. (2012). An improved estimate of microbially mediated carbon fluxes from the Greenland ice sheet. *J. Glaciol.* 58 (212), 1098–1108. doi:10.3189/2012JoG12J001

Darcy, J. L., King, A. J., Gendron, E. M. S., and Schmidt, S. K. (2017). Spatial autocorrelation of microbial communities atop a debris-covered glacier is evidence of a supraglacial chronosequence. *FEMS Microbiol. Ecol.* 93 (8). doi:10.1093/femsec/fix095

Darcy, J. L., and Schmidt, S. K. (2016). Nutrient limitation of microbial phototrophs on a debris-covered glacier. *Soil Biol. biochem.* 95, 156–163. doi:10.1016/j.soilbio.2015.12.019

Deline, P. (2002). "Etude géomorphologique des interactions entre écroulements rocheux et glaciers dans la haute montagne alpine: Le versant sud-est du massif du Mont blanc (vallée d'Aoste, italie),". Ph.D. thesis (Chambéry: Université de Savoie), 365.

Deline, P., Gardent, M., Magnin, F., and Ravanel, L. (2012). The morphodynamics of the mont blanc massif in a changing cryosphere: A comprehensive review. *Geog. Ann. Ser. A* 94 (2), 265–283. doi:10.1111/j.1468-0459.2012.00467.x

Deline, P. (2009). Interactions between rock avalanches and glaciers in the Mont Blanc massif during the late Holocene. *Quat. Sci. Rev.* 28, 1070–1083. doi:10.1016/j.quascirev.2008.09.025

Fairchild, I. J., Bradby, L., Sharp, M., and Tison, J.-L. (1994). Hydrochemistry of carbonate terrains in alpine glacial settings. *Earth Surf. Process.Landf.* 19, 33–54. doi:10.1002/esp.3290190104

Foster, L. A., Brock, B. W., Cutler, M. E. J., and Diotri, F. (2012). A physically based method for estimating supraglacial debris thickness from thermal band remote-sensing data. *J. Glaciol.* 58 (210), 677–691. doi:10.3189/2012JoG11J194

Franzetti, A., Tatangelo, V., Gandolfi, I., Bertolini, V., Bestetti, G., Diolaiuit, G., et al. (2013). Bacterial community structure on two alpine debris-covered glaciers and biogeography of *Polaromonas* phylotypes. *ISME J.* 7, 1483–1492. doi:10.1038/ismej.2013.48

Fyffe, C. L., Brock, B. W., Kirkbride, M. P., Black, A. R., Smiraglia, C., and Diolaiuti, G. (2019a). The impact of supraglacial debris on proglacial runoff and water chemistry. *J. Hydrol.* 576, 41–57. doi:10.1016/j.jhydrol.2019.06.023

Fyffe, C. L., Brock, B. W., Kirkbride, M. P., Mair, D. W. F., Arnold, N. S., Smiraglia, C., et al. (2019b). Do debris-covered glaciers demonstrate distinctive hydrological behaviour compared to clean glaciers? *J. Hydrol.* 570, 584–597. doi:10.1016/j.jhydrol.2018.12.069

Fyffe, C. L., Reid, T. D., Brock, B. W., Kirkbride, M. P., Diolaiuti, G., Smiraglia, C., et al. (2014). A distributed energy-balance melt model of an alpine debris-covered glacier. *J. Glaciol.* 60 (221), 587–602. doi:10.3189/2014JoG13J148

Fyffe, C. L., Woodget, A. S., Kirkbride, M. P., Deline, P., Westoby, M. J., and Brock, B. W. (2020). Processes at the margins of supraglacial debris cover: Quantifying dirty ice ablation and debris redistribution. *Earth Surf. Process. Landforms* 45, 2272–2290. doi:10.1002/esp.4879

Gobbi, M., Isaia, M., and De Bernardi, F. (2011). Arthropod colonisation of a debris-covered glacier. *Holocene* 21 (2), 343–349. doi:10.1177/0959683610374885

Graly, J. A., Drever, J. I., and Humphrey, N. F. (2017). Calculating the balance between atmospheric CO2 drawdown and organic carbon oxidation in subglacial hydrochemical systems. *Glob. Biogeochem. Cycles* 31 (4), 709–727. doi:10.1002/2016GB005425

Gulley, J., and Benn, D. I. (2007). Structural control of englacial drainage systems in Himalayan debris-covered glaciers. *J. Glaciol.* 53 (182), 399–412. Cambridge University Press. doi:10.3189/002214307783258378

Herreid, S., and Pellicciotti, F. (2020). The state of rock debris covering Earth's glaciers. *Nat. Geosci.* 13 (9), 621–627. doi:10.1038/s41561-020-0615-0

Hiller, R., Zeeman, M. J., and Eugster, W. (2008). Eddy-covariance flux measurements in the complex terrain of an Alpine valley in Switzerland. *Boundary-Layer Meteorol.* 127 (3), 449–467. doi:10.1007/s10546-008-9267-0

Hodson, A., Anesio, A. M., Ng, F., Watson, R., Quirk, J., Irvine-Fynn, T., et al. (2007). A glacier respires: Quantifying the distribution and respiration CO2 flux of cryoconite across an entire Arctic supraglacial ecosystem. *J. Geophys. Res.* 112, G04S36. doi:10.1029/2007JG000452

Hodson, A., Anesio, A. M., Tranter, M., Fountain, A., Osborn, M., Priscu, J., et al. (2008). Glacial ecosystems. *Ecol. Monogr.* 78 (1), 41–67. doi:10.1890/07-0187.1

Hodson, A. J., Tranter, M., and Vatne, G. (2000), Contemporary rates of chemical denudation and atmospheric CO_2 sequestration in glacier basins: An Arctic perspective, *Earth Surf. Proc. Land* 25, 1447–1471. doi:10.1002/1096-9837(200012)25:13<1447:AID-ESP156>3.0.CO;2-9

Kirkbride, M. P. (2011). "Debris-covered glaciers," in Encyclopedia of snow, Ice and glaciers. *Encyclopedia of Earth Sciences series*. Editors V. P. Singh, P. Singh, and U. K. Haritashya (Dordrecht: Springer). doi:10.1007/978-90-481-2642-2

Kormann, R., and Meixner, F. X. (2001). An analytical footprint model for non-neutral stratification. *Bound.-Layer Meteor* 99, 207–224. doi:10.1023/A:1018991015119

Manzoni, S., Scimel, J. P., and Porporato, A. (2012). Responses of soil microbial communities to water stress: Results from a meta-analysis. *Ecology* 93, 930–938. doi:10.1890/11-0026.1

Matsuoka, N. (1990). Mechanisms of rock breakdown by frost action: An experimental approach. *Cold Regions Sci. Technol.* 17 (3), 253–270. doi:10.1016/S0165-232X(05)80005-9

Mihalcea, C., Brock, B. W., Diolaiuiti, G., D'Agata, C., Citterio, M., Kirkbride, M. P., et al. (2008). Using ASTER satellite and ground-based surface temperature measurements to derive supraglacial debris cover and thickness patterns on Miage Glacier (Mont Blanc Massif, Italy). *Cold Reg. Sci. Tecnol.* 52, 341–354. doi:10.1016/jcoldregions.2007.03.004

Miles, K. E., Hubbard, B., Irvine-Fynn, T. D. L., Miles, E. S., Quincey, D. J., and Rowan, A. V. (2020). Hydrology of debris-covered glaciers in High Mountain Asia. *Earth-Science Rev.* 207, 103212. doi:10.1016/j.earscirev.2020.103212

Neftel, A., Spirig, C., and Ammann, C. (2008). Application and test of a simple tool for operational footprint evaluations. *Environ. Pollut.* 152 (3), 644–652. doi:10.1016/j.envpol.2007.06.062

Nicholson, L., and Stiperski, I. (2020). Comparison of turbulent structures and energy fluxes over exposed and debris-covered glacier ice. *J. Glaciol.*, 1–13. doi:10.1017/jog.2020.23

Nicholson, L., Wirbel, A., Mayer, C., and Lambrecht, A. (2021). The challenge of non-stationary feedbacks in modeling the response of debris-covered glaciers to climate forcing. *Front. Earth Sci.* 9, 662695. doi:10.3389/feart.2021.662695

Racoviteanu, A. E., Nicholson, L., Glasser, N. F., Miles, E., Harrison, S., and Reynolds, J. M. (2022). debris-covered glacier systems and associated glacial lake outburst flood hazards: Challenges and prospects. *J. Geol. Soc.* 179 (3), jgs2021–084. doi:10.1144/jgs2021-084

Raiswell, R. (1984). Chemical models of solute acquisition in glacial meltwaters. *J. Glaciol.* 30 (104), 49–57. doi:10.3189/S0022143000008480

Reid, T. D., and Brock, B. W. (2010). An energy-balance model for debris-covered glaciers including heat-conduction through the debris layer. *J. Glaciol.* 56, 903–916. doi:10.3189/002214310794457218

Rounce, D. R., Hock, R., McNabb, R. W., Millan, R., Sommer, C., Braun, M. H., et al. (2021). Distributed global debris thickness estimates reveal debris significantly impacts glacier mass balance. *Geophys. Res. Lett.* 48, e2020GL091311. doi:10.1029/2020GL091311

Rowan, A. V., Egholm, D. L., Quincey, D. J., and Glasser, N. F. (2015). Modelling the feedbacks between mass balance, ice flow and debris transport to predict the response to climate change of debris-covered glaciers in the himalaya. *Earth Planet. Sci. Lett.* 430, 427–438. doi:10.1016/j.epsl.2015.09.004

Scherler, D., Bookhagen, B., and Strecker, M. R. (2011). Spatially variable response of himalayan glaciers to climate change affected by debris cover. *Nat. Geosci.* 4, 156–159. doi:10.1038/ngeo1068

Scherler, D., Wulf, H., and Gorelick, N. (2018). Global assessment of supraglacial debris-cover extents. *Geophys. Res. Lett.* 45 (21), 11,798–11,805. doi:10.1029/2018GL080158

Seok, B., Helmig, D., Williams, M. W., Liptzin, D., Chowanski, K., and Hueber, J. (2009). An automated system for continuous measurements of trace gas fluxes through snow: An evaluation of the gas diffusion method at a subalpine forest site, niwot ridge, Colorado. *Biogeochemistry* 95, 95–113. doi:10.1007/s10533-009-9302-3

Sharp, M., Parkes, J., Cragg, B., Fairchild, I. J., Lamb, H., and Tranter, M. (1999). Widespread bacterial populations at glacier beds and their relationship to rock weathering and carbon cycling. *Geology* 27 (2), 107–110. doi:10.1130/0091-7613(1999)027<0107:WBPAGB>2.3.CO;2

Sharp, M., Tranter, M., Brown, G. H., and Skidmore, M. (1995). Rates of chemical denudation and CO drawdown in a glacier-covered alpine catchment. *Geology* 23 (1), 61–64. doi:10.1130/00917613(1995)023<0061:ROCDAC>2.3.CO;2

Shaw, T. E., Brock, B. W., Fyffe, C. L., Pellicciotti, F., Rutter, N., and Diotri, F. (2016). Air temperature distribution and energy-balance modelling of a debris-covered glacier. *J. Glaciol.* 62 (231), 1–14. doi:10.1017//jog.2016.31

Shukla, T., Sundriyal, S., Stachnik, L., and Mehta, M. (2018). Carbonate and silicate weathering in glacial environments and its relation to atmospheric CO_2 cycling in the Himalaya. *Ann. Glaciol.* 59 (77), 159–170. doi:10.1017/aog.2019.5

Steiner, J. F., Lit, M., Stigter, E. E., Shea, J., Bierkens, M. F. P., and Immerzeel, W. W. (2018). The importance of turbulent fluxes in the surface energy balance of a debris-covered glacier in the Himalayas. *Front. Earth Sci.* 6. doi:10.3389/feart.2018.00144

St. Pierre, K. A., Louis, S. T., Schiff, S. L., Lehnherr, I., Dainard, P. G., Gardner, A. S., et al. (2019). Proglacial freshwaters are significant and previously unrecognized sinks of atmospheric CO_2. *Proc. Natl. Acad. Sci. U. S. A.* 116 (36), 17690–17695. doi:10.1073/pnas.1904241116

Telling, J., Anesio, A. M., Tranter, M., Stibal, M., Hawkings, J., Irvine-Fynn, T., et al. (2012). Controls on the autochthonous production and respiration of organic matter in cryoconite holes on high Arctic glaciers. *J. Geophys. Res.* 117, G01017. doi:10.1029/2011JG001828

Tielidze, L. G., Bolch, T., Wheate, R. D., Kutuzov, S. S., Lavrentiev, I. I., and Zemp, M. (2020). Supra-glacial debris cover changes in the Greater Caucasus from 1986 to 2014. *Cryosphere* 14, 585–598. doi:10.5194/tc-14-585-2020

Tranter, M., Brown, G. H., Raiswell, R., Sharp, M. J., and Gurnell, A. M. (1993). A conceptual model of solute acquisition by Alpine glacial meltwaters. *J. Glaciol.* 39, 573–581. doi:10.3189/s0022143000016464

Tranter, M., Sharp, M. J., Lamb, H. R., Brown, G. H., Hubbard, B. P., Willis, I. C., et al. (2002). Geochemical weathering at the bed of Haut Glacier d'Arolla, Switzerland—a new model. *Hydrological processes* 16 (5), 959–993. doi:10.1002/hyp.309

Wadham, J. L., Hawkings, J. R., Tarasov, L., Gregoire, L. J., Spencer, R. G. M., Gutjahr, M., et al. (2019). Ice sheets matter for the global carbon cycle. Nat. Commun*10* 10, 3567. doi:10.1038/s41467-019-11394-4

Wadham, J. L., Tranter, M., Skidmore, M., Hodson, A. J., Priscu, J., Lyons, W. B., et al. (2010). Biogeochemical weathering under ice: Size matters. *Glob. Biogeochem. Cycles* 24, GB3025. doi:10.1029/2009GB003688

Wang, J., Han, H., and Zhang, S. (2014). Carbon dioxide flux in the ablation area of Koxkar glacier, Western Tien Shan, China. *Ann. Glaciol.* 55 (66), 231–238. doi:10.3189/2014AoG66A060

Wang, J., and Xu, J. (2018). CO_2 flux variation and its contribution area in the debris-covered area of Koxkar Glacier, Mt. Tianshan in China. *Environ. Earth Sci.* 77, 611. doi:10.1007/s12665-018-7784-9

Wang, S., Liu, J., Pritchard, H. D., Linghong, K., Qiao, X., Zhang, J., et al. (2023). Characterizing 4 decades of accelerated glacial mass loss in the west Nyainqentanglha Range of the Tibetan Plateau. *HESS* 27, 933–952. doi:10.5194/hess-27-933-2023

Watson, C. S., Quincey, D. J., Carrivick, J. L., and Smith, M. W. (2016). The dynamics of supraglacial ponds in the Everest region, central Himalaya. *Glob. Planet. Change* 142, 14–27. doi:10.1016/j.gloplacha.2016.04.008

Webb, E. K., Pearman, G. I., and Leuning, R. (1980). Correction of flux measurements for density effects due to heat and water vapour transfer. *Q. J. R. Meteorol. Soc.* 106, 85–100. doi:10.1002/qj.49710644707

Westoby, M. J., Rounce, D. R., Shaw, T. E., Fyffe, C. L., Moore, P. L., Stewart, R. L., et al. (2020). Geomorphological evolution of a debris-covered glacier surface. *Earth Surf. Process. Landforms* 45, 3431–3448. doi:10.1002/esp.4973

Yallop, M. L., Anesio, A. J., Perkins, R. G., Cook, J., Telling, J., Fagan, D., et al. (2012). Photophysiology and albedo-changing potential of the ice-algal community on the surface of the Greenland ice sheet. *ISME J.* 6, 2302–2313. doi:10.1038/ismej.2012.107

Yao, J., Gu, L., Han, H., Wang, Y., and Liu, S. (2014). The surface energy budget on the debris-covered Koxkar Glacier in China. *Environ. Earth Sci.* 72, 4503–4510. doi:10.1007/s12665-014-3350-2